Original

Koch, W.; Feser, F.:

Relationship between SAR-Derived Wind Vectors and Wind at 10-m Height Represented by a Mesoscale Model

In: Monthly Weather Review (2006) AMS

DOI: 10.1175/MWR3134.1

Relationship between SAR-Derived Wind Vectors and Wind at 10-m Height Represented by a Mesoscale Model

WOLFGANG KOCH AND FRAUKE FESER

GKSS Research Center Geesthacht, Institute for Coastal Research, Geesthacht, Germany

(Manuscript received 31 January 2005, in final form 26 September 2005)

ABSTRACT

Wind vectors over the ocean were extracted from a large number of synthetic aperture radar (SAR) images from the European Remote Sensing Satellites (*ERS-1* and *ERS-2*). The wind directions are inferred from the orientation of wind streaks that are imaged by the SAR, while the wind speeds are retrieved by inversion of the C-band model CMOD4. The derived wind directions and speeds were compared to wind vectors from the numerical Regional Model (REMO) that are available hourly on a 55-km grid. The large number of comparisons and independent weather situations allowed for an analysis of subsets that are classified by SAR-derived wind speed. A strong decrease of the standard deviation of directional differences with increasing wind speed was found. Biases of directional differences depend on SAR wind speed as well. Furthermore, the influence of the temporal difference between SAR overflight and model and an automatic image filtering on the directional error is demonstrated. Overall, reasonable fields of wind vectors were extracted from SAR imagery in 70 of 80 cases. These fields provide valuable information for validation of numerical models of the atmosphere and case studies of coastal wind fields.

1. Introduction

With the Canadian satellite *Radarsat I* and the European *Envisat*, currently two spaceborne C-band synthetic aperture radar (SAR) instruments are available. *Radarsat II* scheduled to be launched in late 2006, is planned to be in operation for seven years. With a swath width of up to 450 km, considerable coverage of the earth's surface is achieved. The instruments can be used to retrieve wind measurements over the oceans at day and night and all weather conditions because the normalized radar cross section (NRCS), obtained from the calibrated images, is related to wind speed, incidence angle, and wind direction. Experience with previously available SAR instruments showed that standard deviations of 1.5 m s^{-1} (Vachon and Dobson 1996) or 1.8 m s^{-1} (Fetterer et al. 1998; Monaldo et al. 2001) can be achieved in comparison with buoy-measured wind speeds using the buoy wind direction for the wind retrieval. Comparisons with model wind predictions using the model wind direction for SAR wind computation gave somewhat larger numbers (Monaldo et al. 2001). However Horstmann et al. (2003) found an rms error of less than 1.6 m s^{-1} using model directions with a dataset of SAR imagettes covering the global ocean.

The extraction of wind directions directly from the SAR images by means of an analysis of the image spectrum was first attempted in 1986 by Gerling (1986); similar approaches were used by Vachon and Dobson (1996), Fetterer et al. (1998), and Lehner et al. (1998). The opportunity to estimate 180° ambiguous wind directions directly from the SAR image arises, as there are several physical effects causing features that are aligned with the wind direction, for instance, various types of boundary layer rolls (Brown 1980; Alpers and Brümmer 1994; Young et al. 2002), Langmuir cells, surfactant streaks, foam and water blown from breaking waves, or wind shadowing. Standard deviations of the directional differences reported are between 10° and 37° depending on quality control, data, and method used. With the European Remote Sensing Satellite (ERS) scatterometer Stoffelen and Anderson (1997) and Quilfen et al. (1998) achieved standard deviations of 19° and 18.6°, respectively.

It is an open question as to whether wind-aligned signature on SAR images is present frequently enough

Corresponding author address: Wolfgang Koch, GKSS Research Center Geesthacht, Institute for Coastal Research, Max-Planck-Strasse 1, D-21502 Geesthacht, Germany.
E-mail: wolfgang.koch@gkss.de

to be of practical relevance. For instance, investigations of SAR images by Levy and Brown (1998) showed that boundary layer rolls were definitely present in 44% and absent in 34% of 1882 investigated SAR images, while for the remaining 22% the decision was not safe. However, recent work from Dankert et al. (2003) with a real aperture radar showed wind-aligned signatures on scales of 200 m, lasting at least for several tenths of seconds, that should be detectable in images from spaceborne SAR as well and thus might enlarge the fraction of SAR images where wind directions can be extracted. A generating mechanism for such wind streaks was proposed by Drobinski and Foster (2003); they showed these small-scale wind streaks being very closely aligned with the surface wind direction.

The present study searches for relationships between wind-induced patterns on SAR images and wind direction at the 10-m height. Both entities are accessible by proxy data. The wind vectors are approximated by a numerical weather model, while the directions of image patterns are approximated by a method that is based on gradients. Although well-processed measurements are preferable to any numerical weather model winds, it would be very hard to get enough good measurements for a detailed analysis, as intended here. For instance, Vachon and Dobson (1996) used 16 ship measurements corrected for sensor height and shadowing as reference data, while Fetterer et al. (1998) used 61 buoy wind measurements.

Nevertheless, good proxies are needed: Data from model failures or from image patterns not roughly aligned with the local wind should not be used because they contribute no information about the relationships in question, but affect the analysis of the results by introducing random errors.

The SAR images used in this study were acquired by the European Remote Sensing Satellites, *ERS-1* and *ERS-2*, between August 1991 and January 1997. All images are close to coastal areas, mainly from the North Sea and the Baltic Sea. Model results stem from the Regional Model (REMO). They are available on the hour on grid cells of about 55×55 km^2 size. The dense output time step is a great advantage of this model because this allows one to minimize the error due to wind variability. This error cannot be determined a priori, but by comparing with several different model wind fields it is possible to modify the time differences between satellite overflight and model output time and quantify the effects, which are considerable. Other aspects investigated are 1) the influence of a fully automatic image filter on the wind direction retrieval, 2) the impact of SAR-derived wind directions on SAR-derived wind speed, and 3) how often reasonable wind fields can be retrieved from SAR images.

While the emphasis of the present work is on a particular application of the method described in Koch (2004), the results may apply, at least qualitatively, beyond this limit too. Perhaps most important is that reasonable wind fields can be obtained from the vast majority of the SAR images. For this particular method to be able to compute reasonable wind directions, obviously the imprints and the physical phenomena causing them have to be present very frequently. Also important is the decrease of directional differences with increasing wind speeds. This is, to our knowledge, a new finding for SAR wind direction retrieval.

The paper is organized as follows: Section 2 explains the wind determination from SAR images. A description of the numerical weather model REMO is given in section 3, and the comparison is done in section 4.

2. Wind determination based on SAR images

The SAR image products used are precision images (PRI) and single-look complex (SLC) images from the vertical polarized C-band SAR instruments of the European Remote Sensing Satellites *ERS-1* and *ERS-2*. The images were calibrated and corrected for power loss. The algorithms used for the radiometric calibration of ERS SAR images including computation of the incidence angles are given by Laur et al. (1998). Wind from calibrated SAR images is estimated by inverting an empirical function that gives the NRCS as a function of incidence angle, wind direction with respect to radar look direction, and wind speed. The empirical C-band model used in this study is the official European Space Agency (ESA) algorithm CMOD4 (Stoffelen and Anderson 1997). Derivation of wind direction from SAR images comprises three steps:

1) The SAR amplitude images are smoothed and resampled to images with 100-, 200-, and 400-m pixels, and gradients are computed. Additionally, image pixels corresponding to land and some types of nonwind features are identified automatically using a land–sea table and the algorithm given in Koch (2004). The orientation of linear structures extending over several image points is just orthogonal to the gradient and thus 180° ambiguous. Due to the multiplicative noise present in SAR images the computed orientations vary considerably, but there is a preference toward the orientation of the underlying structure.
2) Thus, for the areas of interest, histograms are built. Orientations stemming from the previously identified unusable points are excluded. A histogram of a

sufficient number of orientations will have a peak close to the orientation of the underlying structure.
3) The 180° ambiguity is resolved and one of the suggested directions stemming from the different pixel sizes is selected.

Details of steps 1 and 2 are given in Koch (2004). However, some properties of the method employed should be noted here. The procedure involves several steps of smoothing and image reduction; thus, on the one hand it eases the effects of speckle noise that is pertinent to SAR images. On the other hand, greatest sensitivity is achieved for gradients of structures with a spacing of 400–2000, 800–4000, and 1600–8000 m for 100-m, 200-m, and 400-m pixels, respectively, while structures with sizes below 200 m, 400 m, and 800 m are completely removed. The gradients are used to compute the 180° ambiguous orientations. The latter are used to build one histogram for each subimage of interest and pixel size used. Any orientation in the histogram gets a weight. A good weight is obtained when the orientations are well aligned in a small neighborhood and when the corresponding gradient is strong. This raw histogram is then smoothed and the orientation at the peak is taken as representative for the whole subimage.

This setup was tested with artificial 5×5 km^2 SAR images of unidirectional patterns with fixed and varying wavelengths including SAR typical noise. The obtained orientations are accurate to about 1° except for the images with fixed wavelength of 1 km on 400-m pixels. This failure was to be expected because the sampling is not adequate. The given accuracy holds where the modulation of the patterns is greater than 5% of the mean value. Beyond this limit accuracy degrades and, when the peak of the histogram vanishes in the background noise or when there is no signal at all, the results are random. Under the assumption of a sufficiently strong directional signal aligned with the wind direction being present in a SAR image, this means that the error stemming from the numerical scheme gives only a minor contribution to the overall directional uncertainty. Even the presence of land or nonwind features will do no harm as long as they can be located and there remain enough unaffected orientations to form a reasonable histogram.

In contrast to artificial SAR images, real ones usually will not show unidirectional patterns, but superpositions of various textures. For instance, there may be patterns caused by very long ocean gravity waves, gusts, and marine boundary layer rolls within the same image. In such a case there might be two peaks in the histogram from the 100-m pixels due to ocean waves and gusts, and one peak in each of the other histograms due to the boundary layer rolls. This example illustrates that not every computed orientation will be related to wind. In fact, it is not ensured that there is any wind-aligned pattern present in a particular image. Also, orientations stemming from different wind-related patterns are not necessarily aligned with the wind direction very closely, as is known, for instance, from boundary layer rolls.

In this study the areas of interest in the SAR image were chosen to just cover the corresponding grid cells of REMO. This makes the comparison particularly easy because no spatial interpolation of the obtained directions is necessary. For each such SAR subimage and each pixel size one histogram is built and evaluated, resulting in usually three 180° ambiguous directions to choose from. Different rules may be followed for that choice. One rule is to take the direction closest to the model wind direction; another rule is to take the direction closest to wind-aligned signatures that are visible in the SAR image. Using the first rule makes the method fully automatic and is suited for routine application, but SAR and model wind are not really independent then. Of all possible choices this one will give the best statistics and will be used as reference.

Handling the second rule, closest to wind-aligned signatures, implies visual assessment of the SAR images and, as such, is a subjective method. With this effort we gain independency of SAR and model winds. Furthermore, cases where either the model wind or the SAR wind direction is dubious may be identified and excluded from comparison. In most circumstances wind shadows in the lee of coasts or behind marine structures somewhere on the image allowed us to resolve the 180° ambiguity. Where necessary, synoptic weather maps were consulted. From the different suggested directions, the one aligning best with the wind streaks visible in the SAR image was chosen. In this way at every date, at least for some REMO grid cells, directions could be fixed. The remaining directions were chosen to be closest to those previously selected. Occasionally wind vectors were computed that were inconsistent with surrounding vectors. If there was additional evidence that these outliers were not related to the local wind, they were manually removed. Such evidence could be, for instance, a very small area of the grid cell being covered causing an undersampled histogram or the SAR-derived wind speed being greatly different from its neighbors, but only where we retrieve a matching wind speed from the SAR image when we assume a matching direction for the retrieval. This happened to 17 vectors out of 650, or about 2.6% of the vectors that passed the full quality control and are used for the comparisons in

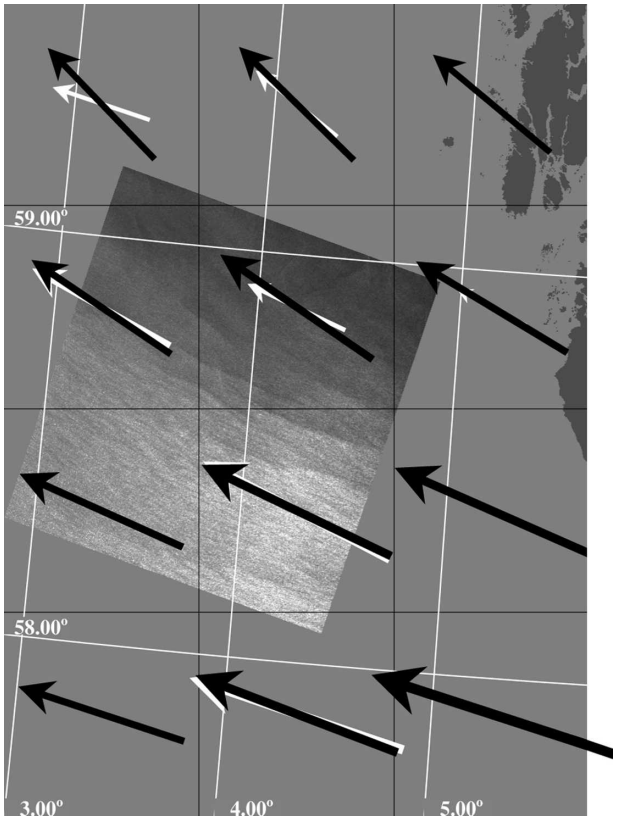

FIG. 1. *ERS-2* SAR image from 1051 UTC 17 Sep 1995. The black arrows indicate wind vectors from the Regional Model, whose grid cell boundaries are identified by the black lines. The wind vectors computed from the SAR image are indicated by the white arrows. The wind speed is 10 m s^{-1} when the arrow length equals the width of one box. Wind streaks are visible in the SAR image and aligned with the model. The dark region is due to the wind shadow cast by the southern tip of Norway just outside the image.

sections 4b and 4c. One of the removed vectors belonged to the third column and third row in Fig. 1, where only a very limited number of gradients were available for the histogram (5, 1, and 0 from 100-m, 200-m, and 400-m pixels, respectively). In contrast, the direction for the second column in the first row was computed from a histogram of 57 gradients from 200-m pixel size. This number is low, but sufficient.

Altogether 159 ERS–SAR products of types PRI and SLC at 80 dates were processed in this way. An additional example for a wind comparison between satellite-derived and modeled wind is plotted in Fig. 2. It shows a strip of four *ERS-1* SAR images from the coast of the Baltic provinces from 0939 UTC 1 October 1995. The strip partially covers a matrix of 3 × 8 grid cells of REMO indicated by black lines. The wind vectors from REMO are indicated by black arrows. The SAR winds are computed from the subimages that correspond to the particular grid cells of REMO. For each subimage the NRCSs and incidence angles of the corresponding image areas, excluding the land points and filtered points, are averaged. The local gradients are computed and define the assumed wind directions. From the different 180° ambiguous estimates of the wind direction provided for each subimage, that one best aligned with the wind streaks visible in the image was selected to compute the SAR wind. The wind vector computed with this direction is indicated by a white arrow. In this case, the chosen wind directions mostly stem from the amplitude images reduced to 200-m pixel size. Although the number of points from the SAR image representing one grid cell of REMO varies considerably and the number of gradients used ranges from 7 to 49 664, the generated wind directions look reasonable and are consistent with REMO and the visible wind streaks.

3. Regional model wind data

For comparison to the satellite-derived wind fields, horizontal winds at a height of 10 m were obtained from a regional model 40-yr run of REMO (Feser et al. 2001; Jacob et al. 1995). REMO is a gridpoint model using a rotated coordinates system. In the vertical, a terrain-following hybrid coordinates system is adopted. A soil model is added to account for soil temperature and water content. The physics scheme applied is a version of the global model ECHAM4 physics adapted for the regional model. The prognostic variables are surface air pressure, horizontal wind components, temperature, specific humidity, and cloud water.

The integration area has a horizontal spherical resolution of 0.5° that corresponds to about 47–55 km in zonal direction and 55 km in meridional direction and includes 81 × 91 grid points. The Arakawa C grid is rotated around Eulerian angles so that the equator is located above the center of the integration domain to achieve a minimum distortion of the grid boxes and to be computational economical. In the vertical, there are 20 hybrid model levels, which are adapted to the orography near the surface.

REMO is forced with the National Centers for Environmental Prediction (NCEP) reanalysis (Kalnay et al. 1996) over the whole integration period from January 1958 to March 1997. These reanalyses include most of the available observational information and are updated every six hours. The horizontal resolution of the analysis is 1.875° (T62 Gaussian grid). Additional to the input data forcing via the lateral boundaries, a spectral nudging technique (von Storch et al. 2000) was applied for the entire model domain. This nudging method keeps the simulated state close to the driving state at

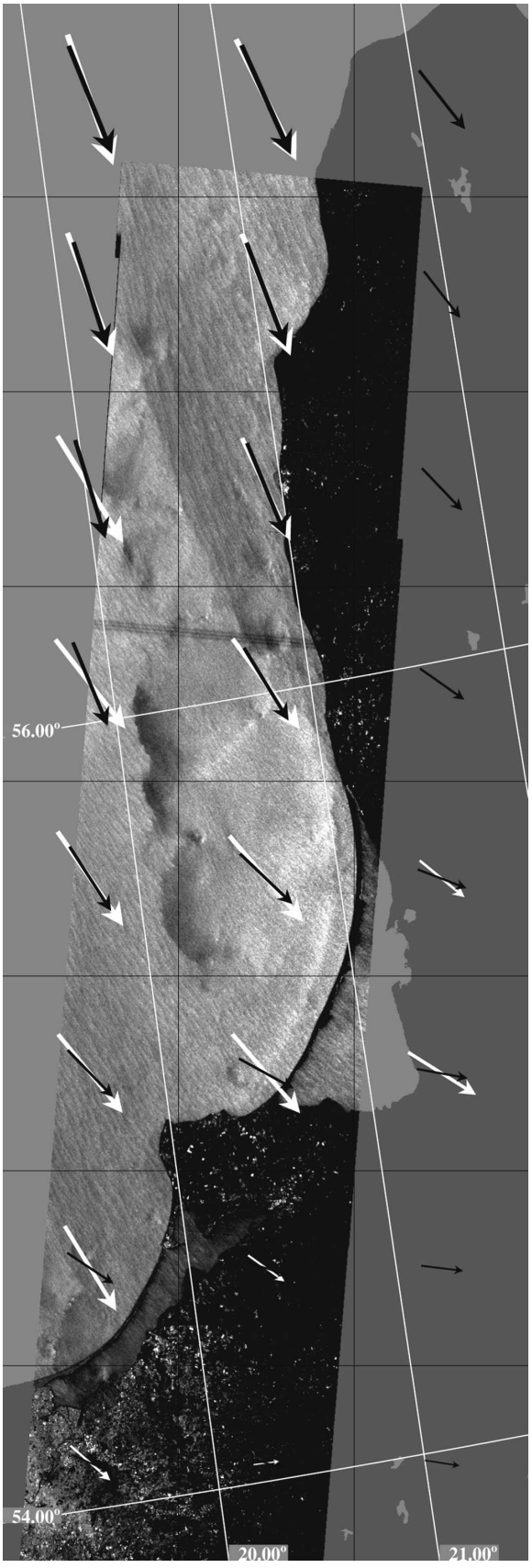

larger scales, while generating regional-scale features independently of the global model.

The 10-m wind used for the comparison is a diagnostic variable. It is calculated from the prognostic surface values and those of the lowest model level at a height of about 32 m, taking into account the topography. The profiles of the variables in the Prandtl layer are based on Monin–Obukhov theory.

The results of the 40-yr run of REMO could have been improved by assimilation of in situ data. However, as constant data quality over the whole integration time was a major issue for the primary application of the model results, no direct data assimilation was performed. Anyhow, by use of the NCEP reanalysis results as forcing, a kind of indirect suboptimal assimilation of in situ data results. This is obvious for the lateral boundaries of the REMO grid where NCEP results are interpolated, but applies as well to the interior of the REMO grid where the assimilation is done by spectral nudging. A validation of REMO with respect to climatological parameters—that is, storm counts—was done by Weisse et al. (2005). Further validation using measurements of wind speed at three sites close to the Dutch coast covering the period from 1985 to 1997 can be found in Weisse et al. (2002). Biases for the three locations range from -0.37 to 0.02 m s^{-1}, while root-mean-square errors are between 2.30 and 3.14 m s^{-1}.

4. Results

The REMO wind fields for the 80 dates were interpolated to match the time of the satellite pass. The interpolation was done by linear interpolation of the magnitudes and the complex units of the Fourier coefficients of the wind fields prior and after the satellite pass. This interpolation generally works well in the interior of the interpolated fields. Problems can arise at the boundaries because the wind fields are nonperiodic. Another problem can occur when features of the wind fields move much more than one grid cell between the interpolated wind fields and the requested time is not close to one of the available times. This would happen in this setup where the speed of a storm or a front as a whole greatly exceeds 55 km h^{-1}. As the SAR images used in this comparison are all situated well inside the REMO grid and the corresponding modeled weather

←

FIG. 2. *ERS-1* SAR images from 0939 UTC 1 Oct 1995. The black arrows indicate wind vectors from REMO, whose grid cell boundaries are identified by the black lines. The wind vectors computed from the SAR image are indicated by the white arrows. The wind speed is 20 m s^{-1} when the arrow length equals the width of one box.

patterns are not moving overly fast, the interpolation is not affected.

a. The discarded dates

As already mentioned in the introduction, bad proxies should not be used to establish the relation between orientations of wind-aligned image features and wind directions at 10-m height. The quality of the proxies is judged for entire scenes because this greatly reduces the number of required decisions and, additionally, makes the decisions less difficult. Altogether, the SAR images from 22 dates were excluded from the comparison. They were carefully scanned for visible wind-aligned structures and separated into three groups. For 12 of these dates there is evidence provided by visible wind streaks or shadows for the SAR-derived wind directions being close to the real wind direction. SAR-retrieved wind vectors should be reasonable here. In most of these cases differences between REMO and SAR wind fields can be reduced, based upon visual assessment, by shifting the REMO wind fields by some grid points or for some hours. Figure 3, for example, shows clear wind streaks aligned with the SAR wind direction; thus, trusting the SAR-derived wind vector in this case, it follows that the model wind vectors do not represent the wind over the coastal waters here. In one case on 1017 UTC 20 November 1996, the REMO wind field indicates a small low pressure system where the SAR-retrieved wind field and a synoptic weather map taken as reference shows an extended low pressure system. In all of these cases SAR-derived wind fields could have improved the modeled ones.

Absence of visible wind-aligned patterns does not necessarily imply that wind directions cannot be extracted from a SAR image. However, in such circumstances, confidence in the SAR-derived wind directions depends solely on their agreement with the model wind direction. Assuming the model wind direction being good, alignment of both directions means there are, indeed, wind-aligned patterns detected by our method. Assuming the model wind direction is bad, alignment of both directions means that the SAR-detected directions are not aligned with the wind and, additionally, model and SAR deviate in the same manner. Although this may happen by chance, it is fairly unlikely. Misalignment of model wind and SAR-derived direction either means that the model wind direction is bad and we have no reference or the SAR-derived direction is not from a wind-aligned pattern and thus should not be used.

On five dates, large portions of the SAR images give no hint of the wind directions. Owing to the lack of detectable wind-aligned image patterns, SAR-derived directions may be unrealistic here. Some wind fields are partially usable, one being a low wind case where the SAR-derived wind speed is usable as it hardly depends on wind direction. Figure 4 shows visible wind streaks only around the island Rügen on the left. On the right side of the image the model wind deviates strongly in direction, rotating left, while SAR directions rotate right. In this case, both SAR and model wind are dubious in the right-hand part of the image.

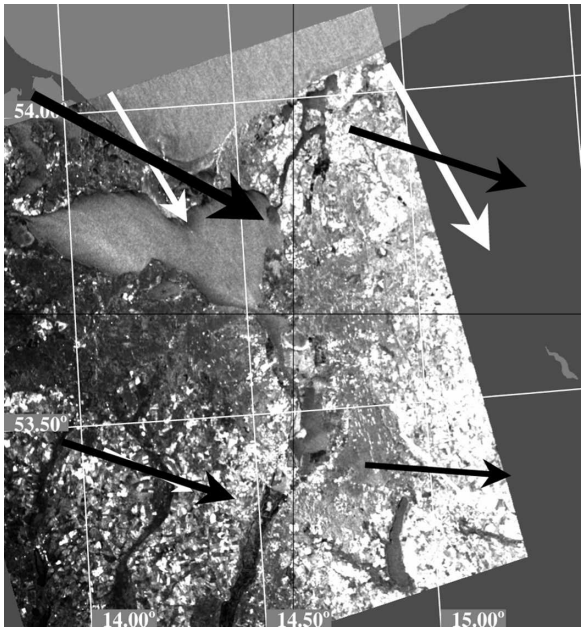

FIG. 3. *ERS-1* SAR image from 2103 UTC 9 Apr 1995, showing clear wind streaks in the Pommerian Bight and in the Odra Lagoon. Wind speed scale is 10 m s^{-1}. The model wind deviates strongly in direction, speed, and gradient of the wind speed; thus, this scene was discarded from the comparison. The model wind field from 3 h later would give a better match.

For the remaining five dates there were no visible clues of wind direction, but there were cellular patterns or ocean waves whose crests were aligned with the SAR-detected directions. Synoptic weather maps agreed better with REMO than with SAR. Here the SAR directions are probably not aligned with the wind, but in spite of that, in one low wind case, the SAR-derived wind speed should still be usable. In another case, shown in Fig. 5, depicting a part of the coast of Iceland, the wind speeds differ greatly. REMO gives 4.3 m s^{-1}, while the smallest possible wind speed retrieved from SAR assuming an upwind situation is 7.3 m s^{-1}. So the model wind speed is much too low, and this raises doubts also about the correctness of the model wind direction. The SAR-retrieved directions are fairly well aligned with each other, but there are none of the typical wind streaks visible in this image, so we do not know whether the SAR directions are aligned with the

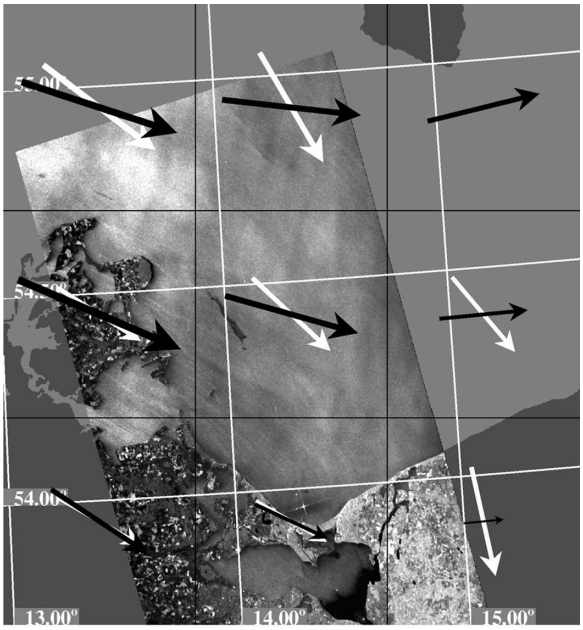

FIG. 4. *ERS-1* SAR image from 2105 UTC 29 Jun 1994, with visible wind streaks only around the island Rügen. Wind speed scale is 10 m s^{-1}. The model wind deviates strongly in direction, rotating left, while SAR directions rotate right; thus, this scene was discarded from the comparison.

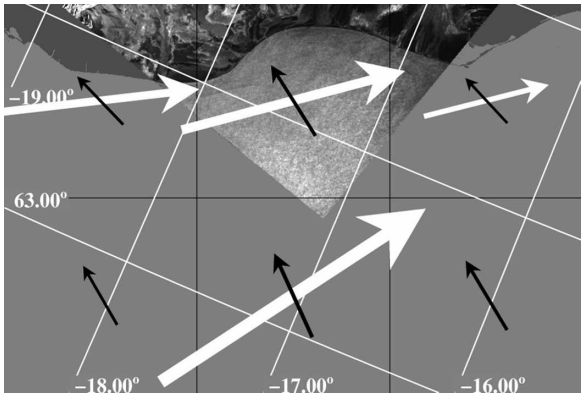

FIG. 5. *ERS-1* SAR image from 1226 UTC 12 Sep 1994. Wind speed scale is 10 m s^{-1}. The model wind deviates strongly in direction and speed from the derived SAR wind. The smallest wind speed that could be retrieved from the SAR image by assuming an upwind situation is 7.3 m s^{-1}. So the model wind speed of about 4.3 m s^{-1} is much too low, raising doubts also about the correctness of the model wind direction. Thus, this scene was discarded from the comparison.

local wind here. We know for sure, however, that the SAR directions are not aligned with the model, even if we term two directions aligned when they are within 45° of each other so that they are more along than crossways. So either the model is greatly wrong or the SAR directions are not aligned with the local wind. In any case these data should be excluded from the comparison.

Consequently 70 of the initially processed 80 dates gave reasonable wind fields. However, investigations of Levy and Brown (1998) showed that boundary layer rolls were present in 44% and absent in 34% of 1882 investigated SAR images. It should be indicated here that none of the 159 processed SAR images is located farther than a few hundred kilometers off the European coasts; thus the sample of SAR images used here may not represent the same situation as was investigated by Levy and Brown (1998). In any case, the large ratio of 87.5% usable SAR wind fields suggests that a considerable fraction of the usable wind patterns is related to other physical phenomena, as for instance the near surface streaks described by Dankert et al. (2003) and Drobinski and Foster (2003). The signatures of near-surface streaks and boundary layer rolls differ in respect to their scale and their alignment with the surface wind direction. While the spacing of near-surface streaks is in the range of hundreds of meters and their directions are almost in line with the surface wind direction, boundary layer rolls have widths of kilometers and their direction is between the surface and the geostrophic wind directions. Thus, in the Northern Hemisphere we expect the roll direction to be rotated clockwise from the surface wind direction on average.

b. Differences between SAR and REMO wind direction

A plain comparison displaying the result that may be expected for unattended computation of SAR wind directions can be done by automatically choosing the SAR direction closest to the model wind direction and neglecting any quality control but the removal of the 17 wind vectors mentioned in section 2. This gives a standard deviation and bias of the directional differences of 23.9° and 1.1°, respectively, and is based on 864 comparisons for 80 dates. Removing the dates with obvious model errors leaves 732 comparisons for 68 dates and yields a standard deviation of 20.3° and a bias of 1.6°. This also gives an idea of what might be gained by SAR wind data assimilation.

By choosing the SAR wind direction closest to wind streak direction for the same dataset we get the statistics of the directional differences between REMO and SAR shown in Table 1. Overall, the standard deviation and bias are 33.2° and 1.9°, respectively. While the bias is not very different, the standard deviation is much larger than before. As we will show below, this comes from the dubious cases discussed in section 4a that are still part of the comparison data in conjunction with the

TABLE 1. Statistics of directional differences REMO − SAR including dubious data. Directions chosen are closest to wind streaks, where possible.

	SAR wind speed range (m s^{-1})							
	2–4	4–6	6–8	8–10	10–12	12–14	14–∞	All
Number of dates used	29	43	38	34	25	14	11	68
Number of comparisons	113	159	167	99	78	77	39	732
Lower 90% confidence bound	0.8	−0.5	−0.1	−10.6	−12.3	−6.8	−5.9	−0.6
Mean (°)	8.1	5.8	5.2	−4.6	−6.6	−4.4	−1.0	1.9
Upper 90% confidence bound	15.3	12.2	10.6	1.3	−0.9	−2.1	3.9	4.3
Lower 90% confidence bound	34.2	36.5	31.6	26.1	21.9	8.8	12.4	31.6
Standard deviation (°)	38.7	40.5	35.0	29.8	25.3	10.2	15.2	33.2
Upper 90% confidence bound	44.5	45.5	39.2	34.6	30.1	12.1	19.6	35.0

selection of the SAR-retrieved direction closest to streaks. Where there are no indications of the wind direction visible in the SAR image, choosing directions closest to streaks is not defined; thus, in these cases we introduce errors at random. Even so, we can already see some properties of the directional differences between REMO and SAR. The standard deviation is largest with 40.5° at the SAR wind speed interval from 4 to 6 m s^{-1} and is lowest with 10.2° for SAR wind speeds between 12 and 14 m s^{-1}. There seems to be a trend for the standard deviations to decrease with increasing wind speed. The widths of the 90% confidence intervals for the standard deviations of directional differences range between 7.2° and 10.3° with no obvious trend. For SAR wind speeds between 12 and 14 m s^{-1} we have 3.3°. Bias ranges from −6.6° to 8.1°, and widths of the corresponding 90% confidence intervals are between 9.8° and 14.5° and one outlier of 4.7°.

After removal of the dubious dates, we get a dataset where we have confidence in the model as well as in the SAR-derived directions. Choosing SAR-derived directions closest to wind streaks yields an overall standard deviation and bias of 17.6° and −0.5° on this subset. Table 2 gives the statistics in dependency from SAR wind speed. From the number of comparisons in Tables 1 and 2 we can see that the additional samples are not equally distributed to the wind speed intervals. Although some of these comparisons are valid measurements, as for instance in Fig. 4, most of them are not and by, using them, in effect we enter a varying fraction of random numbers in our statistic.

Therefore, all statistics and the sensitivity tests in the remainder of this section are based on the 633 pairs of wind vectors stemming from the 58 dates that passed our quality control. It should be noted that under normal operation we would not do such a strict quality control and thus obtain somewhat larger errors. Figure 6 shows the SAR-derived wind speed versus the directional difference between REMO and SAR. Although there are several outliers, the general tendency is a considerably better match of the directions at higher wind speeds. To our knowledge this finding is new for SAR; however, similar behavior was found for the scatterometer, where better directions for higher wind speeds are obtained, because the 3D cone of NRCSs is wider, and thus measurement errors in NRCS do less harm. Table 2 shows the statistics of the directional differences between REMO and SAR. The standard deviation at the lowest SAR wind speed interval from 2 to 4 m s^{-1} is 28.4° and gradually decreases down to 7.7° for SAR

TABLE 2. Statistics of directional differences REMO − SAR with best-quality data. Directions chosen are closest to wind streaks.

	SAR wind speed range (m s^{-1})									
	2–4	4–6	6–8	8–10	10–12	12–14	14–∞	all	4–10	10–14
Number of dates used	24	36	30	31	23	14	10	58	52	23
Number of comparisons	82	127	144	91	74	77	38	633	362	151
Lower 90% confidence bound	2.3	−2.8	−4.7	−3.6	−8.6	−6.8	−1.4	−1.9	−2.6	−6.9
Mean (°)	8.6	0.8	−2.0	−1.3	−6.0	−4.4	1.1	−0.5	−0.9	−5.2
Upper 90% confidence bound	14.8	4.4	0.6	1.0	−3.3	−2.1	3.7	0.8	0.9	−3.4
Lower 90% confidence bound	24.6	18.1	14.4	9.6	9.9	8.8	6.3	16.7	15.6	9.7
Standard deviation (°)	28.4	20.4	16.1	11.0	11.5	10.2	7.7	17.6	16.7	10.8
Upper 90% confidence bound	33.5	23.2	18.2	12.8	13.7	12.1	10.0	18.6	18.0	12.2

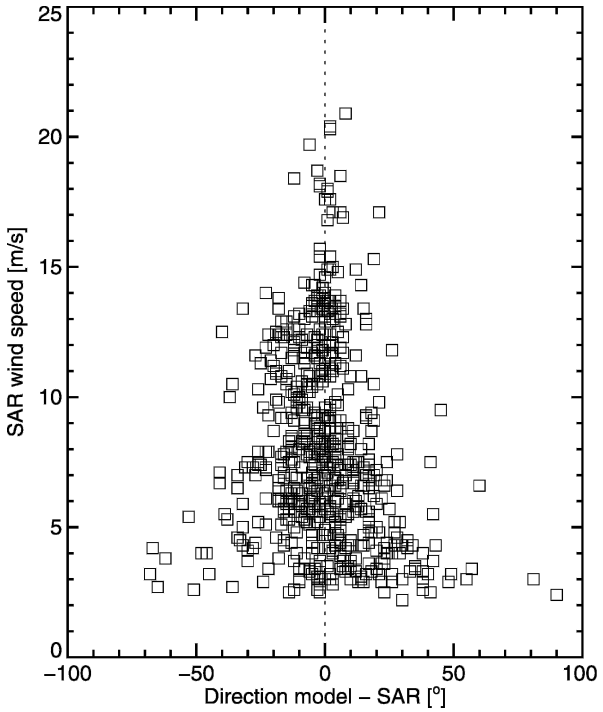

FIG. 6. SAR-derived wind speed in relation to the directional difference using SAR directions closest to wind streaks and the best-quality data.

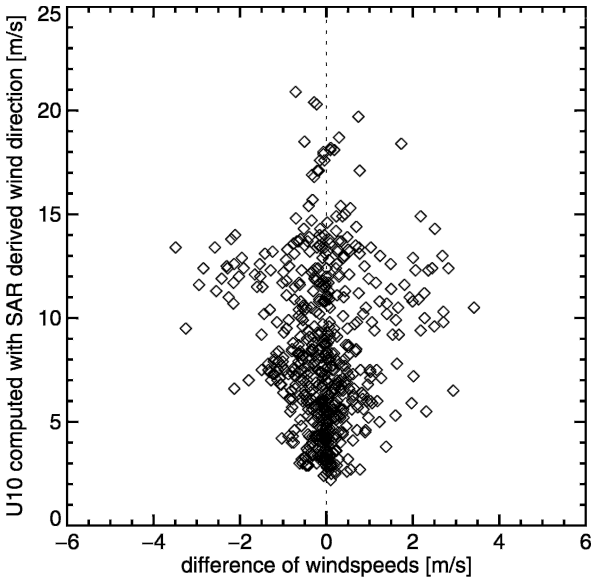

FIG. 7. SAR wind speed computed with SAR-derived wind direction chosen closest to wind streaks vs difference of wind speeds computed from SAR using REMO and SAR-derived wind direction. The plot is based on the best-quality data.

wind speeds above 14 m s^{-1}. The widths of the 90% confidence intervals for the standard deviations of directional differences decreases from nearly 9° for the lowest SAR wind speed interval from 2 to 4 m s^{-1} to below 4° for SAR wind speeds above 6 m s^{-1}. For an idea of the impact of the directional differences Fig. 7 shows the SAR-derived wind speed versus the differences of SAR-derived wind speeds computed with model and with SAR-derived directions. For low wind speeds the large directional differences yield only small variations in the computed wind speed. For moderate and large wind speeds, the sensitivity of the C-band model is increased and so is the quality of the SAR-derived directions.

The range of standard deviations of 10°–37° reported from Gerling (1986), Vachon and Dobson (1996), and Fetterer et al. (1998) is similar to the range of standard deviations of the wind direction differences found for the different wind speed intervals in Tables 1 and 2. Thus, the strong differences of directional accuracy in the literature might to some extent be due to differences in the wind speed distribution of the investigated cases.

The means of the directional differences vary with the wind speed interval. The widths of the 90% confidence intervals starting with 12.5° go down to and remain at about 5°. For SAR wind speeds from 2 to 4 m s^{-1} the complete confidence interval is positive, while for 10 to 14 m s^{-1} it is negative. For the remaining winds speed intervals it is around zero. Contributions to these wind-speed-dependent biases come from SAR processing, direction retrieval method, wind model, physics, and by statistics. We do not know any systematic wind direction bias stemming from the ERS SAR or from REMO, but we know the numerical part of our wind direction retrieval method has no bias and is accurate to 1°. Statistical problems may be caused by a low number of dates or by single dates getting a big weight because they contribute many comparisons to the statistics. The former situation applies for wind speeds above 12 m s^{-1}, and the latter for wind speeds above 12 m s^{-1} and the interval 6–8 m s^{-1}. We may reduce such risks by combining some of the wind speed intervals. For wind speeds of 4–10 m s^{-1} the 90% confidence interval is still around zero and for 10–14 m s^{-1} it is still negative. Neglecting any bias that might be contributed by the ERS SAR and REMO and assuming the biases being due to physical reasons we get the following: For very low wind speeds up to 4 m s^{-1} the wind-induced patterns are rotated counterclockwise. Patterns caused at wind speeds from 4 to 10 m s^{-1} and above 14 m s^{-1} are nearly in line with the wind, and patterns caused at wind speeds from 10 to 14 m s^{-1} are on average rotated clockwise. This would correspond, for instance, to near-surface streaks and boundary layer

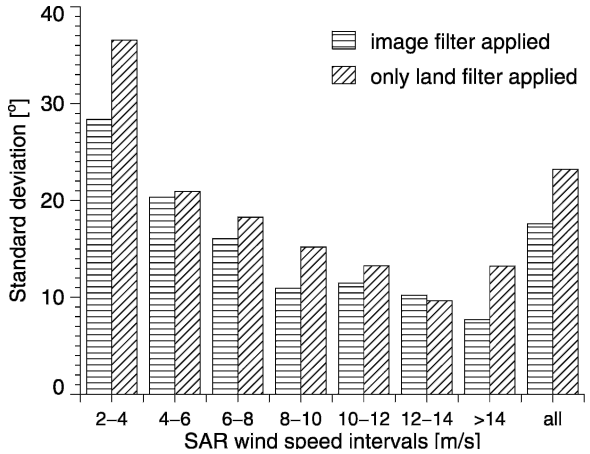

FIG. 8. Influence of the fully automatic image filtering on the standard deviation of the directional differences REMO − SAR, based on the best-quality data and SAR directions chosen closest to wind streaks.

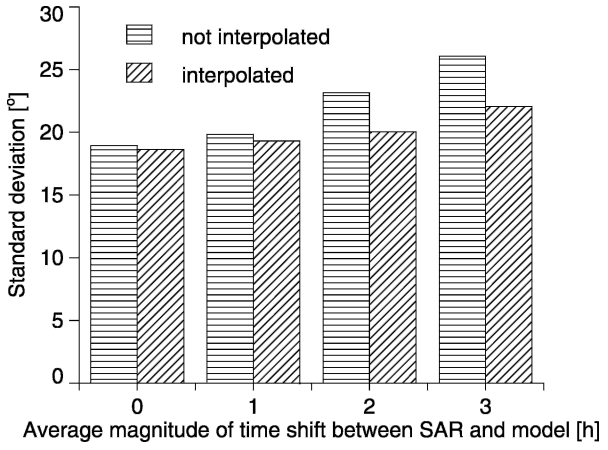

FIG. 9. Standard deviation of the directional difference REMO – SAR dependent upon timing. The model grid cell size is about 55 × 55 km^2. This plot is based on the best-quality data and SAR-derived directions chosen closest to wind streaks.

rolls in the Northern Hemisphere. However, a rotation of about 5° is smaller than expected for average boundary layer rolls. Evaluating all data in one block gives a negligible bias of −0.5° in a confidence interval of only 2.7° width, suggesting no significant bias being present throughout the whole wind speed range.

1) EFFECT OF IMAGE FILTERING

Examples of disturbing image features at high wind speeds are the image artifacts in the fourth row of the grid cells in Fig. 2. They could be misinterpreted as wind streaks if this part of the image was not removed. The automatic localization of such image parts with the algorithm given in Koch (2004) is called filtering. In this case we would get a wind speed of 9.5 m s^{-1} instead of 13 m s^{-1} by wrongly assuming an up or down wind situation. Other disturbing features treated with the image filter are, for instance, caused by sea ice, dry tidelands, atmospheric fronts, surface slicks, or internal waves. Figure 8 shows the effect of the image filtering on the directional error. The horizontally hatched bars give the standard deviation of the directional differences between REMO and SAR-derived wind directions when the image filtering is applied. The diagonally hatched bars give the results when only the land points are excluded. In all but one of the wind speed intervals the directional error is larger when only the land is filtered out. The large impact of the filtering at low wind speeds is due to the high frequency of disturbing image features in these situations (Donelan and Pierson 1987; Lehner et al. 2000). In total, the increase of the standard deviation for all wind speeds seems to be small, but the additional variance introduced by omission of the filtering accounts for approximately 15° standard deviation.

2) INFLUENCE OF TIMING

The delay between model output time and time of satellite image acquisition is an obvious source of error. As the REMO output is available on the hour, it is possible to study this influence by comparing the satellite-derived wind directions with model wind directions from differently delayed model outputs. Along the way the benefits of interpolation, as sketched above in the beginning of section 4, are checked. The horizontally hatched bars in Fig. 9 show the standard deviation of directional differences at the closest REMO outputs and the outputs at one, two, and three hours prior and after the closest one, respectively. Although the increase in the standard deviation appears to be small, the additional variance introduced by a wrong timing of three hours, as could occur when using synoptic wind fields, corresponds to a standard deviation of about 18°. This value should depend on the geographic area under consideration because it reflects the persistence of the weather situations that were imaged. A timing error of more than one hour yields a significant increase and should be avoided. The diagonally hatched bars give the standard deviations that correspond to interpolated model outputs. Here a timing error of two hours is acceptable on average, but in particular cases—for instance, fast-moving storms or fronts—the additional directional error would be much larger than on average. Note that with smaller model grid size the influence of the timing is expected to be even stronger. This emphasizes the importance of temporally dense model outputs.

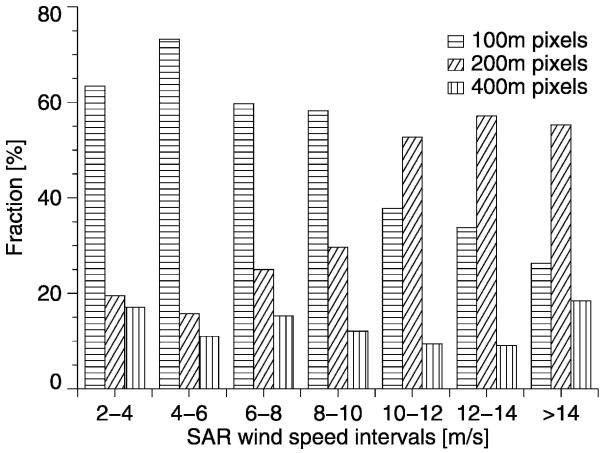

FIG. 10. Percentage of most adequate pixel size for retrieving SAR wind direction, depending on SAR-derived wind speed. This plot is based on the best-quality data and SAR-derived directions chosen closest to wind streaks.

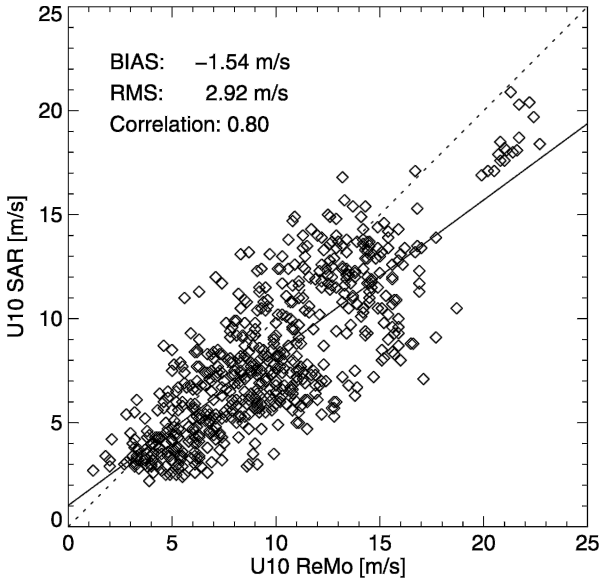

FIG. 11. Wind speed derived from SAR using directions closest to wind streaks vs REMO wind speed. This plot is based on the best-quality data.

3) SPACING OF WIND-ALIGNED IMAGE PATTERNS

Some information on the spacing of the wind-aligned patterns is provided by the pixel size used for the computation of the best-aligned SAR wind direction. Figure 10 shows the percentage of most adequate pixel size for retrieving SAR wind direction, depending on SAR-derived wind speed. Directions from 100-m pixels are most frequently chosen for wind speeds below 10 m s^{-1}. Above 10 m s^{-1}, directions from 200-m pixels are the largest fraction. Directions from 400-m pixels contribute at most 20% to the chosen directions. For pixel sizes of 100, 200, and 400 m, greatest sensitivity is achieved for linear image features with lateral spacing of 400–2000, 800–4000, and 1600–8000 m, while structures with sizes below 200, 400, and 800 m are completely removed.

It is noticeable that at 10 m s^{-1} there is not only the changeover to bigger pixel sizes, but also the transit from strict alignment to clockwise rotation of the detected image patterns; thus, it seems that a different physical mechanism comes into operation at this wind speed.

c. Differences between SAR and REMO wind speed

1) EFFECT OF WIND DIRECTIONS ON WIND SPEED

Figure 11 shows the SAR-derived wind speed versus REMO wind speed for the same 58 dates that were used in section 4b. There is a considerable bias and the rms error is large, while the correlation is fair. Figure 12 shows SAR wind speed computed with REMO wind direction versus REMO wind speed. The figures are quite similar but there is a slight improvement of the statistics due to the SAR-derived wind directions. From the differences of the rms errors, the contribution of the wind directions can be estimated to be about 0.8 m s^{-1}. The small difference in the rms errors suggests that the error due to wind directions may be neglected, but Fig. 7 shows that for many cases wind direction has great impact.

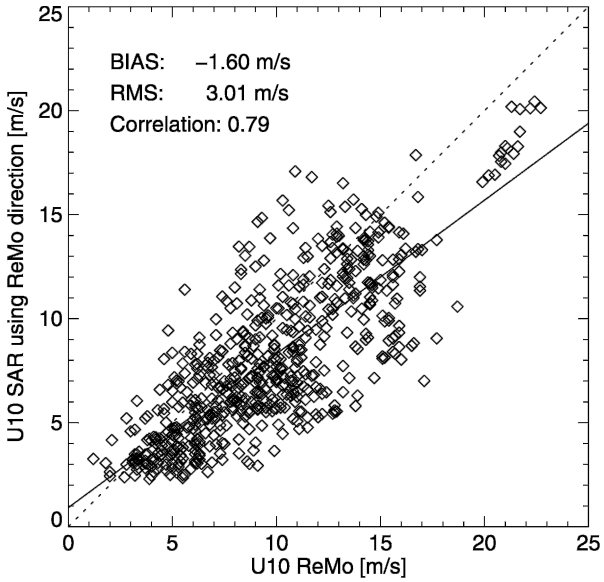

FIG. 12. SAR wind speed computed with model directions vs REMO wind speed. This plot is based on the best-quality data.

2) POSSIBLE REASONS FOR THE LARGE WIND SPEED DIFFERENCES

Bias and rms error given in Fig. 11 are quite large compared to the rms error for ERS scatterometer wind speeds of 1.38 m s^{-1} with negligible bias, reported in Quilfen et al. (1998). Similar results, however, were found by Horstmann et al. (2000, 2002) and Monaldo et al. (2001) who compared *Radarsat-1* scan SAR-retrieved wind fields to numerical models in coastal areas. Two mechanisms cause increased differences between SAR and REMO wind speeds. The REMO treats grid cells as land that include a land portion of more than 50%, and, as the bottom friction is much larger on land, the wind speed is reduced in these cases. The SAR wind speed, however, is computed from the open waters portion of that grid cells and is thus larger, particularly where the wind direction is parallel or toward the coast. The other effect comes from averaging the NRCS. Where there is a nonhomogeneous wind speed inside a model grid cell, averaging the NRCS yields an intermediate wind speed. Atmospheric fronts, far-reaching wind shadows, or coastal jets are examples for such inhomogeneous situations. An example for such a situation is shown in Fig. 1. The model, however, represents such situations by a spatial shift of the extreme wind speeds to the closest grid cell. Thus, in such situations, the SAR wind is either too high where the model wind speed is low or too low where the model wind speed is high. For models with smaller grid cell size the ratio of grid cells matching the aforementioned conditions is smaller; thus differences between SAR and model wind speed could be reduced with grid cell size.

5. Summary

Directions from streaklike patterns were extracted from SAR images of the European coastal waters and compared to wind directions obtained from the mesoscale numerical weather model REMO. The conformance of the wind fields was improved by filtering the SAR images for land and signatures not related to wind direction with an automatic method and by interpolating the model wind fields to the SAR overflight time. Summary statistics were computed for the complete dataset and for a subset without obvious model errors, while a strictly quality controlled subset was taken for closer investigation. Directional ambiguities of the SAR-derived wind vectors were removed semiautomatically by choosing the SAR direction closest to wind streaks.

For the best-quality dataset standard deviations of directional differences decrease with increasing wind speed from 28.4° down to 7.7°. Bias is less than 9° in magnitude, varying in sign and magnitude with wind speed. For SAR wind speeds smaller than 4 m s^{-1} the wind-induced patterns detected in the SAR image are rotated counter clockwise from the wind direction at 10-m height. For 4–10 m s^{-1} patterns and wind directions are in line, while for 10–14 m s^{-1} the patterns are rotated 5° clockwise from the wind direction. For wind speeds greater than 14 m s^{-1} pattern and wind directions seem to be in line again. The transition in the bias at a wind speed of 10 m s^{-1} is accompanied by preferred detection of a wind-induced pattern with a larger lateral spacing.

With a bias of -1.54 m s^{-1} and rms error of 2.92 m s^{-1} the comparison of wind speeds is similar to other comparisons between SAR-derived and modeled wind speeds. As the comparison is done on grid cells of about 55 km, it is affected by subscale effects caused by the structure of the European coasts being treated differently by SAR wind retrieval and the model. Modeling on finer grids would reduce the portion of grid cells affected by subscale effects and should improve the comparison.

SAR direction retrieval using local gradients permits the areawide retrieval of both wind direction and speed with spaceborne active microwave instruments directly at the shore. In 87.5% of the considered dates, reasonable wind fields were derived from the SAR images that are suited for validation of numerical atmospheric models, or process studies, allowing advanced use, for instance, of Envisat and Radarsat.

Acknowledgments. This work was enabled by the German Bundesministerium für Bildung und Forschung (BMBF) in the framework of the project ENVOC, and by ESA, who supplied *ERS-1* and *ERS-2* SAR data under the Announcements of Opportunity AO2.D113 and AOE.220.

REFERENCES

Alpers, W., and B. Brümmer, 1994: Atmospheric boundary layer rolls observed by the synthetic aperture radar aboard the ERS-1 satellite. *J. Geophys. Res.,* **99,** 12 613–12 621.

Brown, R., 1980: Longitudinal instabilities and secondary flows in the planetary boundary layer: A review. *Rev. Geophys. Space Phys.,* **18,** 683–697.

Dankert, H., J. Horstmann, and W. Rosenthal, 2003: Ocean wind fields retrieved from radar-image sequences. *J. Geophys. Res.,* **108,** 3352, doi:10.1029/2003JC002056.

Donelan, M., and W. Pierson, 1987: Radar scattering and equilibrium ranges in wind-generated waves with application to scatterometry. *J. Geophys. Res.,* **92,** 4971–5029.

Drobinski, P., and R. C. Foster, 2003: On the origin of near-

surface streaks in the neutrally-stratified planetary boundary layer. *Bound.-Layer Meteor.,* **108,** 247–256.

Feser, F., R. Weisse, and H. von Storch, 2001: Multi-decadal atmospheric modeling for Europe yields multi-purpose data. *Eos, Trans. Amer. Geophys. Union,* **82,** 305–310.

Fetterer, F., D. Gineris, and C. Wackerman, 1998: Validating a scatterometer wind algorithm for ERS-1 SAR. *IEEE Trans. Geosci. Remote Sens.,* **36,** 479–492.

Gerling, T., 1986: Structure of the surface wind field from Seasat SAR. *J. Geophys. Res.,* **91,** 2308–2320.

Horstmann, J., W. Koch, S. Lehner, and R. Tonboe, 2000: Wind retrieval over the ocean using synthetic aperture radar with C-band HH polarization. *IEEE Trans. Geosci. Remote Sens.,* **38,** 2122–2131.

——, ——, ——, and ——, 2002: Ocean winds from RADARSAT-1 ScanSAR. *Can. J. Remote Sens.,* **28,** 524–533.

——, H. Schiller, J. Schulz-Stellenfleth, and S. Lehner, 2003: Global wind retrieval from SAR. *IEEE Trans. Geosci. Remote Sens.,* **41,** 2277–2286.

Jacob, D., R. Podzun, and M. Claussen, 1995: REMO—A model for climate research and weather prediction. *Proc. Int. Workshop on Limited-Area and Variable Resolution Models,* Beijing, China, WMO, 273–278.

Kalnay, E., and Coauthors, 1996: The NCEP/NCAR 40-Year Reanalysis Project. *Bull. Amer. Meteor. Soc.,* **77,** 437–471.

Koch, W., 2004: Directional analysis of SAR images aiming at wind direction. *IEEE Trans. Geosci. Remote Sens.,* **42,** 702–710.

Laur, H., P. Bally, P. Meadows, S. J. B. Schättler, and E. Lopinto, 1998: Derivation of the backscattering coefficient σ_0 in ESA ERS-1/2.SAR.PRI data products. Tech. Note ES-TN-RS-PM-HL09, issue 2, Revision 5b, ESA, Frascati, Italy, 47 pp.

Lehner, S., J. Horstmann, W. Koch, and W. Rosenthal, 1998: Mesoscale wind measurements using recalibrated ERS SAR images. *J. Geophys. Res.,* **103,** 7847–7856.

——, J. Schulz-Stellenfleth, B. Schättler, H. Breit, and J. Horstmann, 2000: Wind and wave measurements using complex ERS-2 SAR wave mode data. *IEEE Trans. Geosci. Remote Sens.,* **38,** 2246–2257.

Levy, G., and R. A. Brown, 1998: Detecting planetary boundary layer rolls from SAR. *Remote Sensing of the Pacific Ocean from Satellites,* R. A. Brown, Ed., Earth Ocean and Space, 128–134.

Monaldo, F., D. Thompson, R. Beal, W. Pichel, and P. Clemente-Colon, 2001: Comparison of SAR-derived wind speed with model predictions and ocean buoy measurements. *IEEE Trans. Geosci. Remote Sens.,* **39,** 2587–2600.

Quilfen, Y., B. Chapron, T. Elfouhaily, K. Katsaros, and J. Tournadre, 1998: Observation of tropical cyclones by high-resolution scatterometry. *J. Geophys. Res.,* **103,** 7767–7786.

Stoffelen, A., and D. Anderson, 1997: Scatterometer data interpretation: Estimation and validation of the transfer function CMOD4. *J. Geophys. Res.,* **102,** 5767–5780.

Vachon, P. W., and F. Dobson, 1996: Validation of wind vector retrieval from ERS-1 SAR images over the ocean. *Global Atmos. Ocean Syst.,* **5,** 177–187.

von Storch, H., H. Langenberg, and F. Feser, 2000: A spectral nudging technique for dynamical downscaling purposes. *Mon. Wea. Rev.,* **128,** 3664–3673.

Weisse, R., F. Feser, and H. Gunther, 2002: A 40-year high-resolution wind and wave hindcast in the southern North Sea. *Proc. Seventh Int. Workshop on Wave Hindcasting and Forecasting,* Banff, AB, Canada, Department for the Environment, Canada Meteorological Service, 97–104.

——, H. von Storch, and F. Feser, 2005: Northeast Atlantic and North Sea storminess as simulated by a regional climate model during 1958–2001 and comparison with observations. *J. Climate,* **18,** 465–479.

Young, G. S., D. A. R. Kristovich, M. R. Hjelmfelt, and R. C. Foster, 2002: Rolls, streets, waves, and more: A review of quasi-two-dimensional structures in the atmospheric boundary layer. *Bull. Amer. Meteor. Soc.,* **83,** 997–1001.